Bilobate comet morphology and internal structure controlled by shear deformation

C. Matonti, N. Attree, O. Groussin, L. Jorda, S. F. Hviid, S. Bouley, D. Nébouy, A.-T. Auger, Philippe Lamy, H. Sierks, et al.

nature geoscience

ARTICLES

https://doi.org/10.1038/s41561-019-0307-9

Bilobate comet morphology and internal structure controlled by shear deformation

C. Matonti[1,2*], N. Attree[1,3], O. Groussin[1], L. Jorda[1], S. Viseur[2], S. F. Hviid[4], S. Bouley[5], D. Nébouy[1], A.-T. Auger[1], P. L. Lamy[1,6], H. Sierks[7], G. Naletto[8,9,10], R. Rodrigo[11,12], D. Koschny[13], B. Davidsson[14], M. A. Barucci[15], J.-L. Bertaux[6], I. Bertini[8], D. Bodewits[16], G. Cremonese[17], V. Da Deppo[10], S. Debei[18], M. De Cecco[19], J. Deller[7], S. Fornasier[15], M. Fulle[20], P. J. Gutiérrez[21], C. Güttler[7], W.-H. Ip[22,23], H. U. Keller[24,4], L. M. Lara[21], F. La Forgia[8], M. Lazzarin[8], A. Lucchetti[17], J. J. López-Moreno[21], F. Marzari[8], M. Massironi[25,9], S. Mottola[4], N. Oklay[4], M. Pajola[17], L. Penasa[9], F. Preusker[4], H. Rickman[26,27], F. Scholten[4], X. Shi[7], I. Toth[28], C. Tubiana[7] and J.-B. Vincent[4]

Bilobate comets—small icy bodies with two distinct lobes—are a common configuration among comets, but the factors shaping these bodies are largely unknown. Cometary nuclei, the solid centres of comets, erode by ice sublimation when they are sufficiently close to the Sun, but the importance of a comet's internal structure on its erosion is unclear. Here we present three-dimensional analyses of images from the Rosetta mission to illuminate the process that shaped the Jupiter-family bilobate comet 67P/Churyumov–Gerasimenko over billions of years. We show that the comet's surface and interior exhibit shear-fracture and fault networks, on spatial scales of tens to hundreds of metres. Fractures propagate up to 500 m below the surface through a mechanically homogeneous material. Through fracture network analysis and stress modelling, we show that shear deformation generates fracture networks that control mechanical surface erosion, particularly in the strongly marked neck trough of 67P/Churyumov–Gerasimenko, exposing its interior. We conclude that shear deformation shapes and structures the surface and interior of bilobate comets, particularly in the outer Solar System where water ice sublimation is negligible.

Following classical dynamical scenarios[1], comets were formed during the early stages of the Solar System, and have since been stored far from the Sun in a very cold environment, either in the Kuiper belt or in the Oort cloud. They hold clues with which to constrain the formation and evolution of the Solar System, including insights into prebiotic molecular chemistry. Comet 67P/Churyumov–Gerasimenko (hereafter 67P), studied here, is a Jupiter family comet that originates from the Kuiper belt.

During its two years of orbiting comet 67P, Rosetta's cameras have acquired thousands of images revealing its bilobate nature[2]. Bilobate comets can be formed by either the low-velocity (metres per second) accretion of two primordial objects[3,4], or the re-aggregation of material after a later rotational breakup of the nucleus[5] or even catastrophic collision[6,7] that can happen multiple times. Such a configuration seems to be common for comets, since four of the seven spatially resolved nuclei are bilobate. Understanding erosion processes on cometary nuclei and how these processes modify their global shape is key to constraining their internal structure and evolution.

The OSIRIS-NAC[8] image resolution (down to <20 cm per pixel) allowed for detailed geological interpretations and in particular led to the observation of pervasive arrays of lineaments existing at all scales (from centimetres to hectometres), some of which have been interpreted as layers[2,3] and others as fractures[9–11]. Whereas the metre-scale polygonal fractures originate from thermal stress[11,12], a large population of fractures tens to hundreds of metres long still remains, of unknown origin. Lineaments are mainly observed in the southern hemisphere, which exhibits fewer than or no dust deposits compared with the northern hemisphere[13], and therefore shows more continuous outcrops of brittle material, prone to fracturing (Fig. 1a).

[1]Aix Marseille Université, CNRS, CNES, LAM, Marseilles, France. [2]Aix Marseille Université, CNRS, IRD, INRA, Coll France, CEREGE, RRH, Aix-en-Provence, France. [3]Faculty of Natural Sciences, University of Stirling, Stirling, UK. [4]Deutsches Zentrum für Luft- und Raumfahrt (DLR), Institut für Planetenforschung, Berlin, Germany. [5]GEOPS—Géosciences Paris Sud, Université Paris-Sud, CNRS, Université Paris-Saclay, Orsay, France. [6]LATMOS, CNRS/UVSQ/IPSL, Guyancourt, France. [7]Max Planck Institute for Solar System Research, Göttingen, Germany. [8]University of Padova, Department of Physics and Astronomy "Galileo Galilei", Padua, Italy. [9]University of Padova, Center of Studies and Activities for Space (CISAS) "G. Colombo", Padua, Italy. [10]CNR-IFN UOS Padova LUXOR, Padua, Italy. [11]Centro de Astrobiologia, CSIC-INTA, Torrejon de Ardoz, Madrid, Spain. [12]International Space Science Institute, Bern, Switzerland. [13]Science Support Office, European Space Research and Technology Centre/ESA, Noordwijk, The Netherlands. [14]Jet Propulsion Laboratory, M/S 183-401, Pasadena, CA, USA. [15]LESIA, Observatoire de Paris, Université PSL, CNRS, Univ. Paris Diderot, Sorbonne Paris Cité, Sorbonne Université, Meudon, France. [16]Physics Department, Auburn University, Auburn, AL, USA. [17]INAF, Astronomical Observatory of Padova, Padua, Italy. [18]University of Padova, Department of Industrial Engineering, Padua, Italy. [19]University of Trento, Faculty of Engineering, Trento, Italy. [20]INAF Astronomical Observatory of Trieste, Trieste, Italy. [21]Instituto de Astrofisica de Andalucìa (CSIC), Granada, Spain. [22]Graduate Institute of Astronomy, National Central University, Chung-Li, Taiwan. [23]Space Science Institute, Macau University of Science and Technology, Taipa, Macao. [24]Institut fur Geophysik und Extraterrestrische Physik, Technische Universität Braunschweig, Braunschweig, Germany. [25]University of Padova, Department of Geosciences, Padua, Italy. [26]Department of Physics and Astronomy, Uppsala University, Uppsala, Sweden. [27]PAS Space Research Center, Warsaw, Poland. [28]Konkoly Observatory, Budapest, Hungary. *e-mail: matonti.christophe@free.fr

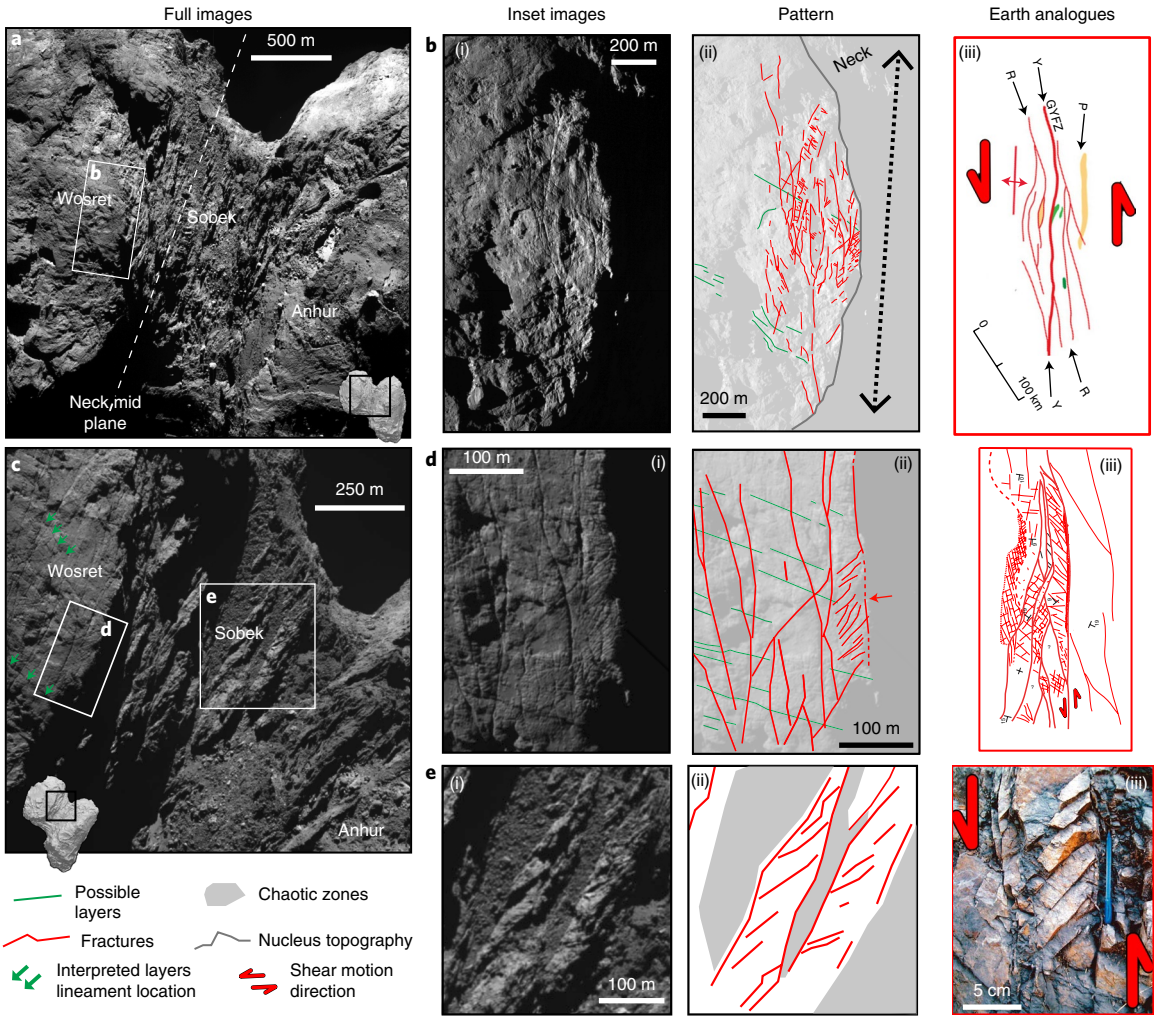

Fig. 1 | Fracture pattern on 67P's southern hemisphere showing fracture interpretations and comparison with typical Earth analogues or equivalents. **a**, NAC_2016-01-28T05.33.00.986Z_ID30_1397549000_F22 image, showing neck borders and centre regions (white box shows the location of panel b view). **b**, NAC_2016-01-30T08.28.39.721Z_ID30_1397549200_F22 image, showing the Wosret neck border (i) with interpreted layers (green) and digitalized fracture lineaments (red), revealing anastomosing and highly interconnected patterns (ii); also shown is an Earth example of a fault-zone showing a similar anastomosing pattern and following typical Riedel-shear structure (with R&P and Y planes)[18] (iii). **c**, NAC_2016-01-27T18.20.08.974Z_ID30_1397549000_F22 cropped image, showing close-up of the neck centre, exhibiting ridges and chaotic zones. **d**, Zoom on the neck border (i) with fractures (red) cross-cutting possible layers (green), highlighting the occurrence of a dense, oblique fracture set located between longer fractures (ii) and an example of an anastomosing shear fault zone with sinistral-slip motion, including oblique shear fractures between minor fault and sheared block[19] (iii). **e**, Close-up of brittle material ridges in the neck bottom (i), affected by oblique fractures (in red) and chaotic/unstructured crushed zones (in grey) (ii) and an image of a sheared rock block, pinched between two minor faults, exhibiting oblique Riedel-shear fractures (iii). Panels reproduced from: **b**(iii), ref. [18], Elsevier; **e**(iii), ref. [21], Elsevier. Panel **d**(iii) adapted from ref. [19], Elsevier. Credit: (**a**, **b**(i), **b**(ii), **c**, **d**(i), **d**(ii) and **e**(i)): ESA/Rosetta/MPS for OSIRIS Team MPS/UPD/LAM/IAA/SSO/INTA/UPM/DASP/IDA

Hectometre to kilometre fracture networks near the neck

In the southern hemisphere neck and neck-border regions (Fig. 1a and Supplementary Figs. 1 and 3–5) we observed two types of lineaments tens to hundreds of metres long. Type 1 lineaments (green in Fig. 1) are continuous and parallel to each other (green arrow in Fig. 1c,Fig. 1d and Supplementary Fig. 5). These lineaments follow the topography contour lines and are therefore sub-parallel to the surface (Supplementary Section 2.1 and Supplementary Figs. 5 and 7c,d), which agrees well with their previous interpretation and modelling as possible layers[3,14].

Type 2 lineaments (red in Fig. 1) are composed of two sets, each with a preferential direction. They show the following attributes: (1) high interconnectivity and bent extremities (Fig. 1b(ii),d(ii)); (2) discontinuous and curvilinear; (3) cross cut, hence postdate, type-1 lineaments (Fig. 1d(i),(ii)). Type 2 lineaments cut straight across contour lines and are consequently sub-vertical to the surface (Fig. 1b,c, Supplementary Figs. 3, 4 and 7 and Supplementary Sections 1.1, 2.1 and 2.2). From these characteristics, and following the geological principles of initial horizontality[15] and cross-cutting relationship[16], type 2 lineaments cannot be primordial features such as layers, but are structural discontinuities, that is, fractures or faults.

Evidence for shear deformation

In addition to the above basic attributes defining fractures, type 2 lineaments show strong evidence for shearing. Fracture terminations such as branching structures or imbricated fans observed in the Geb and Atum regions (Fig. 1 and Supplementary Figs. 3 and 4) are typical of fractures or faults developed in a shear context[17].

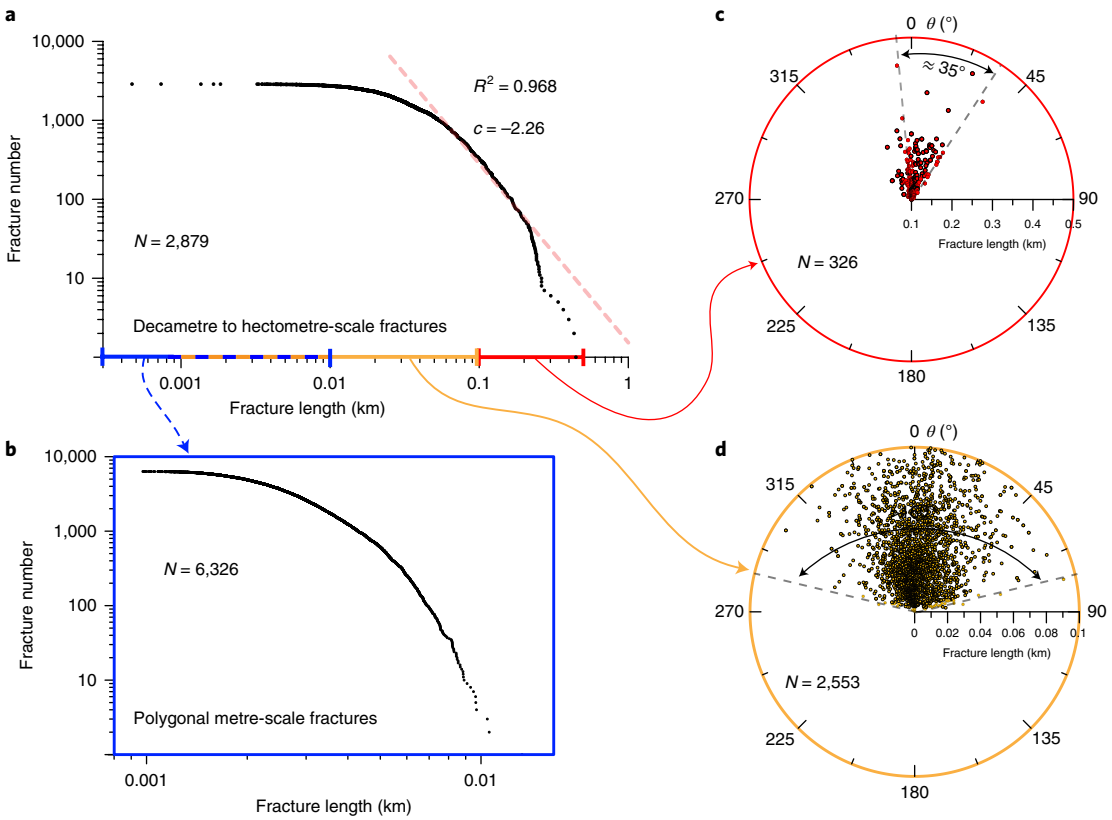

Fig. 2 | Fracture length distribution and direction statistics. a, Cumulative length distribution plot of all the digitalized fractures (with R^2 the determination coefficient and c the power law index of the fit). The distribution follows a power law between 30–40 m and 250 m (see Methods). **b**, Cumulative length distribution of metre-scale polygonal fractures (data from ref. [11]) showing no evidence of a power-law distribution, but exponential distribution, unlike tectonic shear (linked or reactivated) fractures and faults, which classically exhibit power-law distribution. **c**, Polar plot of the average directions of the longest fractures ($L > 100$ m) compared to the neck middle plane (angle $\theta = 0°$ means parallel to the neck). It shows scattering mainly over a range of 35°. **d**, Polar plot of the shorter fracture ($L < 100$ m) directions compared to the neck middle plane. It shows large scattering over a range exceeding 100°.

In the Wosret and Anhur regions at the neck's border, an anastomosing fracture pattern with numerous interconnections (Fig.1b–d and Supplementary Fig. 5), along with bends of one fracture extremity towards another, indicates mechanical interaction and also suggests a shear context[18–20] (Supplementary Fig. 3b and Fig. 1b(iii), d(iii)). In Sobek and Neith, in the neck's central regions, we observe highly fractured sheared block structures[21], alternating with unstructured areas composed of metre-scale (possibly less) blocks (Fig. 1c,e (i)–(iii) and Supplementary Section 2.3). Possible metre-scale offsets of previously formed lineaments (fractures or layers) in the Geb region clearly point to fault-like planes existing on 67P (Supplementary Fig. 3c and Supplementary Section 1).

The evolution of these fracture and fault structures towards the neck's centre, from branching and anastomosing networks in the neck border to sheared blocks and crushed-chaotic zones in the neck centre (Figs. 1c,e, Supplementary Fig. 6a and Supplementary Section 2.3), suggests an increasing deformation gradient. This observation is fully consistent with classical fault/sheared-zone models on Earth, where the maximum strain is located at its centre[22] (Supplementary Fig. 6b).

If the shearing process is a valid interpretation, fracture patterns should follow geologically relevant geometry. To further assess this geometry and reinforce the evidence for shearing, we performed a quantitative analysis of the lengths and directions of 2,879 fractures. The fracture lengths vary from 0.5 m to 450 m. The fracture cumulative length distribution follows a power law between 30 m and 250 m, with a power index of −2.3 (Fig. 2a). Such a distribution is typical of fractures and faults on Earth[23], and this index is moreover mainly characteristic of fractures formed or reactivated in shear[24]. The 326 longest fractures (>100 m, Fig. 2c) are all strictly orientated within 35° of the neck midplane direction[25] (see Methods) and form characteristic diamond-shaped patterns visible in both hemispheres (Supplementary Figs. 7c,d, 8c and 9) following two preferential directions separated by 30–40° (Fig. 2c,d). Such a pattern matches very well with the occurrence of a Riedel-shear deformation structure between the lobes[26–28] that can exist at all scales (Supplementary Fig. 8a,d and Supplementary Section 2.4). The measured 30°–40° angle between Riedel-shear fractures should correspond to the internal friction angle of the material (Supplementary Fig. 8a), which fully agrees with values estimated for 67P using surface morphologies and modelling[5,29,30].

Interestingly, the length distribution of the smallest (<30 m) fractures does not follow a power law, as well as the polygonal metre-scale fractures (Fig. 2b), and shows a large scattering in directions of almost 180° (Fig. 2d). Both of these observations support a different origin for these fractures[31], more likely thermal fracturing instead of 'tectonic-like' shearing.

Finally, we developed a stress model for 67P[32] (see Methods), which indicates that the maximum differential stress, of up to 450 Pa, occurs in the neck regions (Supplementary Fig. 10a). This value exceeds the estimated bulk nucleus (tensile or shear) strength of typically 1–100 Pa[33,34], thus allowing fracturing. Shear stress is also maximum near the neck centre (>100 Pa, Supplementary Fig. 10b) and in the neck's perpendicular direction, which is compatible with

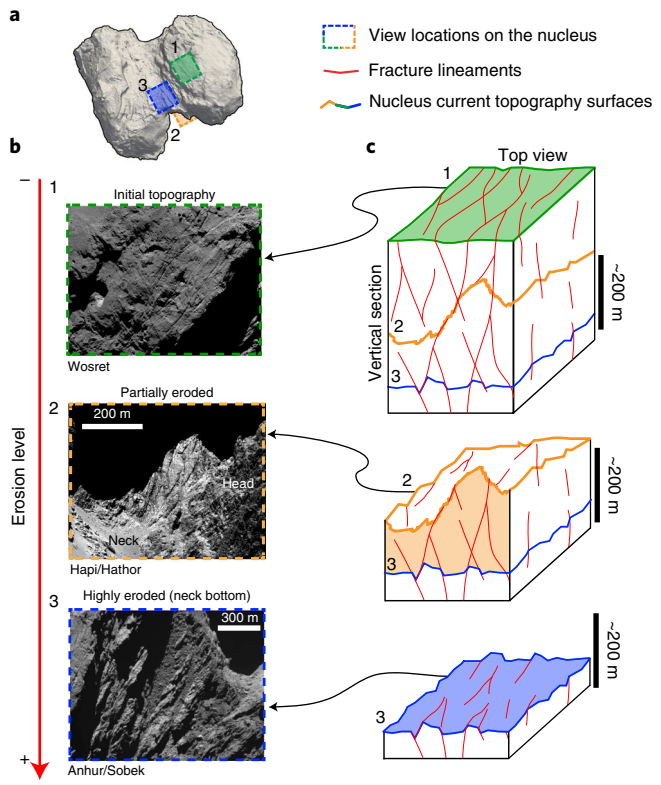

Fig. 3 | Block diagram revealing 67P's fractured internal structure and its evolution through increasing mechanical erosion. a, Location of the three views of 67P's nucleus. **b**, OSIRIS-NAC images illustrating increasing erosion level along a unique fractured structure. **c**, Block diagrams: (1) initial, non (mechanically) eroded topographic surface, as observed in the Wosret region; (2) partially eroded topographic surface, cut along the pre-existing fracture directions and dip angles, as observed in the Hapi equatorial area (Bakhu); (3) highly flattened surface topography, eroded along the same fracture network with increased deformation in the centre of the neck, forming lenticular-shaped ridges and crushed chaotic zones, as observed in the Anhur/Sobek regions. Credit: (**b**): ESA/Rosetta/MPS for OSIRIS Team MPS/UPD/LAM/IAA/SSO/INTA/UPM/DASP/IDA

the location and directions of the observed shear deformations. Such stress is caused by torque at the neck boundary, owing to the fact that the neck plus the head lobe is cantilevered over 67P's centre of gravity and is falling onto it with a twisting motion.

To summarize, all the above observations and models cannot be explained by thermal processes and instead demonstrate the occurrence of a global shear deformation taking place all around the neck, which is mostly independent of solar insulation and has been active far from the Sun, possibly over billions of years[4], since 67P became bilobate.

Constraining the nucleus internal structure

The global shear stress not only implies surface deformation, but also a strain in the whole nucleus interior. To assess this hypothesis, we studied fractures along the vertical direction, relative to the local gravity vector (that means, along their height instead of their strike), and thus probing the nucleus internal structure.

Fractures observed vertically on cliffs in the northern hemisphere's equatorial region (hereafter Bakhu, Supplementary Figs. 7a,b and 9b and Supplementary Sections 2.4 and 3) show maximum heights of 120–190 m. Considering a maximum length of 450 m, this gives fracture length-to-height ratios of around $L/H = 2.36–3.75$ (Fig. 3), typical for fractures and faults on Earth, especially non-layer-restricted ones ($1.8 < L/H < 3.8$)[35].

Fractures on the neck borders (Wosret and Anhur) and the neck's deepest point (Sobek) exhibit similar patterns and sheared block structures (Figs. 1c,e(ii) and SupplementarySections 2.2 and 2.3). This observation proves that they propagate towards the nucleus interior, being part of the same network, and that shearing occurs inside the nucleus, down to at least several hundreds of metres, that is to say, the maximum neck depth (Fig. 3).

In both hemispheres, the neck borders exhibit cliff faces (Supplementary Figs. 7c,d and 9b) that mainly follow the two preferential directions of fractures (Supplementary Fig. 8b). These particular cliffs are thus the remains of fracture walls, where the opposite side has been eroded. Therefore, the nucleus material breakdown, and then erosion, in the neck (that is, the neck's trough shaping) has been, at least partially, caused by shear deformation. Indeed, mechanical breakdown may act or have acted as an amplification/facilitating process for increasing sublimation, by exposing more pristine, non-dust-covered material that is more prone to sublimation and may also have allowed block removal and transport or escape.

These observations imply that from the neck border to the neck centre/bottom, we are observing the same shear structure over hundreds of metres of depth, at different evolution levels, driven by mechanical erosion along underlying and pre-existing fractures (Fig. 3). It goes from fractured with little mechanical erosion in the neck borders (1 in Fig. 3b,c), to partially eroded in Bakhu (2 in Fig. 3b,c), and finally to highly sheared/crushed and eroded, forming flattened areas, in the neck centre (3 in Fig. 3b,c). These three-dimensional (3D) observations necessarily imply that (1) the nucleus interior is structured by decametre-to-hectometre fracture networks; (2) the nucleus material remains sufficiently brittle below the surface to allow fracturing even at depths of several hundreds of metres; (3) although the nucleus exhibits layering, it is mechanically homogeneous enough for fractures to propagate freely, without being stopped or damped by mechanical boundaries, that means that layers do not show sharp mechanical contrasts.

Implications for the evolution of bilobate comets

With these results, we can now propose a chronology explaining the erosion and shape evolution of 67P (Fig. 4). Following ref. [4], 67P acquired its bilobate shape roughly 4.5 billion years ago, in the primordial or scattered disk, through the low-velocity accretion of two cometesimals[4,5] (Fig. 4a). Alternatively, the bilobate shape could also originate from a more recent catastrophic collision and re-accumulation event[6], although the probability of such an event drops to <5% after 3.5 billion years ago[36], when the Kuiper belt acquired its current object density[37] (Fig. 4a).

In the next step, due to torque stress at the lobes' boundary, which originates from an initial asymmetry of the nucleus, shear deformation started all around 67P, leading to pervasive fracturing (that is, type 2 lineaments; Fig. 4b). This stress originated from the geometry of the nucleus, but we cannot exclude that several later close encounters with giant planets[1] provided additional tidal stresses. Continuing shear deformation, possibly over billions of years, progressively increased the fracturing level (length, connections), producing even more broken/damaged material in the neck.

Hundreds of thousands to millions of years ago[1], 67P entered the giant planet region. Its temperature slowly increased and sublimation of the most volatile ices (CO, N_2 and CO_2) began (Fig. 4c). The still-ongoing mechanical breakdown induced by shearing continued to weaken the nucleus material, setting the conditions for differential erosion focused on the lobe boundary, increasing its depth, and forming a deep 'neck' (Fig. 4c). Along with broad volatile sublimation, outbursts induced by fracturing[38] (or fracture and faults

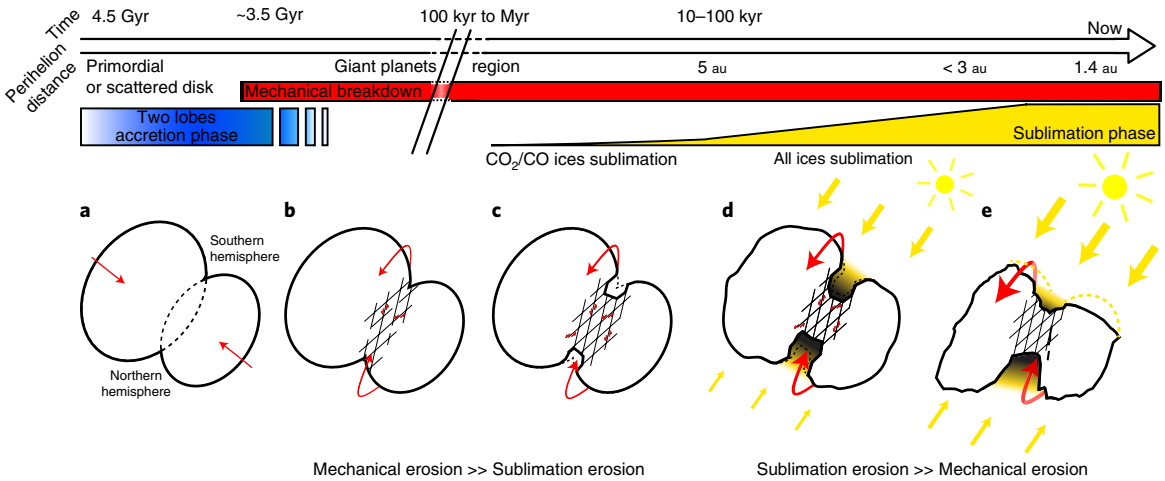

Fig. 4 | Chronology of the evolution of the shape of 67P (from a primordial or collisional later event), showing the effects of the two complementary erosion processes (mechanical erosion and sublimation erosion). The diagrams highlight the contrast between the shear deformation, acting in the neck over long timescales (billions of years), and the sublimation erosion, acting on the broad nucleus over shorter timescales (millions of years). Double red arrows are the symbol for shear deformation, illustrating torque at the neck, and do not imply a sense of rotation.

reactivation), driven by sudden confinement or pressure loss, could also have contributed to ejecting and eroding the fractured loose blocks from the nucleus, enhancing the preferential neck erosion. This process is especially plausible and most efficient for smaller blocks in the crushed material of the neck centre. This led to increasing cliff heights surrounding the neck, and therefore to a higher probability of cliff collapse[39] and block fragmentation, exposing ice-rich materials to the surface, which amplified the preferential erosion in the neck even more.

Finally, 67P reached the inner Solar System and its Jupiter-family comet orbit, with a perihelion distance, q, inside 5 atronomical units (au). At this distance, the sublimation of water ice began, leading to broad erosion by sublimation, which became the dominant process here (Fig. 4d). Reaching its current orbit ($q = 1.2$ au), the erosion was typically 0.4–1 m per orbit[40,41]. This significant erosion primarily affected the most insolated areas at perihelion, that is, the southern hemisphere[40], and more precisely the lobes rather than the neck, where projected shadows limit insolation. It is responsible for the large depth difference between the southern hemisphere (about 450 m) and northern hemisphere (about 930 m), by flattening the southern hemisphere neck's flanks, giving 67P its current north–south asymmetric shape (Fig. 4e).

The above scenario and conclusions about the internal structure are not restricted to 67P, which probably has a shape that is common among cometary nuclei; they could apply to other bilobate comets, possibly also explaining previous (even when not directly observed) nucleus splitting[42]. As shown by the recent New Horizons mission, active geological processes exist in the Kuiper belt, on long timescales, and comets are no exception. This work also provides new insights into the comet activity phenomenon, through which deep propagating fractures and faults growth could trigger outbursts[38], even at large (>5 au) heliocentric distances[43].

Online content

Any methods, additional references, Nature Research reporting summaries, source data, statements of data availability and associated accession codes are available at https://doi.org/10.1038/s41561-019-0307-9.

Received: 20 June 2018; Accepted: 11 January 2019;
Published online: 18 February 2019

References

1. Duncan, M., Levison, H. & Dones, L. in *Comets II* 193–204 (Univ. Arizona Press, Tucson, 2004).
2. Sunshine, J. M., Thomas, N., El-Maarry, M. R. & Farnham, T. L. Evidence for geologic processes on comets. *J. Geophys. Res. Planets* **121**, 2194–2210 (2016).
3. Massironi, M. et al. Two independent and primitive envelopes of the bilobate nucleus of comet 67P. *Nature* **526**, 402–405 (2015).
4. Davidsson, B. J. R. et al. The primordial nucleus of comet 67P/Churyumov-Gerasimenko. *Astron. Astrophys.* **592**, A63 (2016).
5. Hirabayashi, M. et al. Fission and reconfiguration of bilobate comets as revealed by 67P/Churyumov-Gerasimenko. *Nature* **534**, 352–355 (2016).
6. Schwartz, S. R. et al. Catastrophic disruptions as the origin of bilobate comets. *Nat. Astron.* **2**, 379–382 (2018).
7. Jutzi, M. & Benz, W. Formation of bi-lobed shapes by sub-catastrophic collisions. A late origin of comet 67P's structure. *Astron. Astrophys.* **597**, A62 (2017).
8. Keller, H. U. et al. OSIRIS – The scientific camera system onboard Rosetta. *Space Sci. Rev.* **128**, 433–506 (2007).
9. El-Maarry, M. R. et al. Fractures on comet 67P/Churyumov-Gerasimenko observed by Rosetta/OSIRIS. *Geophys. Res. Lett.* **42**, 5170–5178 (2015).
10. Thomas, N. et al. The morphological diversity of comet 67P/Churyumov-Gerasimenko. *Science* **347**, aaa0440 (2015).
11. Auger, A. T. et al. Meter-scale thermal contraction crack polygons on the nucleus of comet 67P/Churyumov-Gerasimenko. *Icarus* **301**, 173–188 (2017).
12. Attree, N. et al. Thermal fracturing on comets. *Astron. Astrophys.* **610**, A76 (2018).
13. Lee, J. C. et al. Geomorphological mapping of comet 67P/Churyumov-Gerasimenko's Southern hemisphere. *Mon. Not. R. Astron. Soc.* **462**, S573–S592 (2016).
14. Penasa, L. et al. A three dimensional modelling of the layered structure of comet 67P/Churyumov-Gerasimenko. *Mon. Not. R. Astron. Soc.* **469**, S741–S754 (2017).
15. Lyell, C. & Deshayes, G. P. *Principles of Geology: Being an Attempt to Explain the Former Changes of the Earth's Surface, by Reference to Causes Now in Operation* (J. Murray, London, 1830).
16. Steno, N. *De Solido Intra Solidum Naturaliter Contento dissertationis prodromus* Vol. 78 (Accademia della Crusca, Florentiae, 1669).
17. Twiss, R. J. & Moores, E. M. *Structural Geology* (W. H. Freeman and Company, New York, 1992).
18. Rao, G. et al. Co-seismic Riedel shear structures produced by the 2010 M_w 6.9 Yushu earthquake, central Tibetan Plateau, China. *Tectonophysics* **507**, 86–94 (2011).
19. Matonti, C., Lamarche, J., Guglielmi, Y. & Marié, L. Structural and petrophysical characterization of mixed conduit/seal fault zones in carbonates: example from the Castellas fault (SE France). *J. Struct. Geol.* **39**, 103–121 (2012).
20. Peacock, D. C. P., Nixon, C. W., Rotevatn, A., Sanderson, D. J. & Zuluaga, L. F. Glossary of fault and other fracture networks. *J. Struct. Geol.* **92**, 12–29 (2016).

21. Mukherjee, S. *Atlas of Structural Geology* (Elsevier Science, Amsterdam, 2015).
22. Mitchell, T. M. & Faulkner, D. R. The nature and origin of off-fault damage surrounding strike-slip fault zones with a wide range of displacements: a field study from the Atacama fault system, northern Chile. *J. Struct. Geol.* **31**, 802–816 (2009).
23. Soliva, R. & Schultz, R. A. Distributed and localized faulting in extensional settings: insight from the NorthEthiopian Rift–Afar transition area.*Tectonics* **27**, TC2003 (2008).
24. Cladouhos, T. T. & Marrett, R. Are fault growth and linkage models consistent with power-law distributions of fault lengths? *J. Struct. Geol.* **18**, 281–293 (1996).
25. Preusker, F. et al. The global meter-level shape model of comet 67P/Churyumov-Gerasimenko. *Astron. Astrophys.* **607**, L1 (2017).
26. Riedel, W. Zur Mechanik Geologischer Brucherscheinunger.*Zentralbl. Mineral. Geol. Paläontol.* **8**, 354–368 (1929).
27. Bartlett, W. L., Friedman, M. & Logan, J. M. Experimental folding and faulting of rocks under confining pressure. 9. Wrench faults in limestone layers. *Tectonophysics* **79**, 255–277 (1981).
28. Ahlgren, S. G. The nucleation and evolution of Riedel shear zones as deformation bands in porous sandstone. *J. Struct. Geol.* **23**, 1203–1214 (2001).
29. Groussin, O. et al. Gravitational slopes, geomorphology, and material strengths of the nucleus of comet 67P/Churyumov-Gerasimenko from OSIRIS observations. *Astron. Astrophys.* **583**, A32 (2015).
30. Vincent, J. B. et al. Constraints on cometary surface evolution derived from a statistical analysis of 67P's topography. *Mon. Not. R. Astron. Soc.* **469**, S329–S338 (2017).
31. Hatton, C. G., Main, I. G. & Meredith, P. G. Non-universal scaling of fracture length and opening displacement. *Nature* **367**, 160–162 (1994).
32. Hviid, S. et al. A creaking and cracking comet. In *AAS/Division for Planetary Sciences Meeting Abstracts* Vol. 48, 211.05 (AAS, 2016).
33. Attree, N. et al. Tensile strength of 67P/Churyumov–Gerasimenko nucleus material from overhangs. *Astron. Astrophys.* **611**, A33 (2018).
34. Basilevsky, A. T. et al. Estimating the strength of the nucleus material of comet 67P Churyumov–Gerasimenko. *Solar Syst. Res.* **50**, 225–234 (2016).
35. Hooker, J. N., Laubach, S. E. & Marrett, R. Fracture-aperture size—frequency, spatial distribution, and growth processes in strata-bounded and non-strata-bounded fractures, Cambrian Mesón Group, NW Argentina. *J. Struct. Geol.* **54**, 54–71 (2013).
36. Durda, D. D. & Stern, S. A. Collision rates in the present-day Kuiper Belt and Centaur regions: applications to surface activation and modification on comets, Kuiper Belt objects, Centaurs, and Pluto–Charon. *Icarus* **145**, 220–229 (2000).
37. Weissman, P. R. & Levison, H. F. in *The Population of the Trans-Neptunian Region: the Pluto-Charon Environment* 559 (Univ. Arizona Press, Tucson, 1997).
38. Skorov, Y. V., Rezac, L., Hartogh, P., Bazilevsky, A. T. & Keller, H. U. A model of short-lived outbursts on the 67P from fractured terrains. *Astron Astrophys.* **593**, A76 (2016).
39. Pajola, M. et al. The pristine interior of comet 67P revealed by the combined Aswan outburst and cliff collapse. *Nat. Astron.* **1**, 0092 (2017).
40. Lai, I. L. et al. Gas outflow and dust transport of comet 67P/Churyumov-Gerasimenko. *Mon. Not. R. Astron. Soc.* **462**, S533–S546 (2016).
41. Keller, H. U. et al. Insolation, erosion, and morphology of comet 67P/Churyumov-Gerasimenko. *Astron. Astrophys.* **583**, A34 (2015).
42. Boehnhardt, H. in *Comets II* 301–316 (Univ. Arizona Press, Tucson, 2004).
43. Sekanina, Z., Larson, S. M., Hainaut, O., Smette, A. & West, R. M. Major outburst of periodic comet Halley at a heliocentric distance of 14 AU. *Astron. Astrophys.* **263**, 367–386 (1992).

Acknowledgements

OSIRIS was built by a consortium of the Max-Planck-Institut für Sonnensystemforschung, Göttingen, Germany; the CISAS University of Padova, Italy; the Laboratoire d'Astrophysique de Marseille, France; the Instituto de Astrofisica de Andalucia, CSIC, Granada, Spain; the Research and Scientific Support Department of the ESA, Noordwijk, Netherlands; the Instituto Nacional de Técnica Aeroespacial, Madrid, Spain; the Universidad Politéchnica de Madrid, Spain; the Department of Physics and Astronomy of Uppsala University, Sweden; and the Institut für Datentechnik und Kommunikationsnetze der Technischen Universität Braunschweig, Germany. The support of the national funding agencies of Germany (DLR), France (CNES), Italy (ASI), Spain (MEC), Sweden (SNSB), and the ESA Technical Directorate is gratefully acknowledged. We thank the Rosetta Science Operations Centre and the Rosetta Mission Operations Centre for the successful rendezvous with comet 67 P/Churyumov–Gerasimenko. We also thank Emerson E&P Software, Emerson Automation Solutions, for providing SKUA-GOCAD licenses in the scope of the Emerson Grant Program, V. A. La Bruna for the interesting Structural Geology discussions related to this study, and Y. Guglielmi for his advices on the submission.

Author contributions

C.M. led this study, mapped the lineaments, performed geological interpretation and wrote most of the manuscript. N.A. performed the 3D projection of the lineaments as well as the statistical calculations and interpretations, and participated in the manuscript writing. O.G. contributed significantly to the interpretations and to the manuscript writing. L.J. provided local and global 3D models and developed tool for images selection and data projection. S.V. contributed to the 3D statistical analysis and data importing to the Gocad software. S.F.H. provided the 3D stress model for 67P. S.B. contributed to improved design of the study, interpretations and manuscript. D.N. contributed to the local and global 3D shape model creation. A.-T.A. contributed to the image selection and geological interpretation. P.L. provided the stereo anaglyph images used for interpretation. H.S., G.N., R.R., D.K. and B.D. are the lead scientists of the OSIRIS project. The other authors are all co-investigators who built and ran this instrument and made the observations possible, and associates and assistants who participated in the study.

Competing interests

The authors declare no competing interests.

Additional information

Supplementary information is available for this paper at https://doi.org/10.1038/s41561-019-0307-9.

Reprints and permissions information is available at www.nature.com/reprints.

Correspondence and requests for materials should be addressed to C.M.

Methods

Analytical methods. Ten OSIRIS-NAC images, acquired between 8.3 km and 70 km from the nucleus centre of mass, were used for this work in order to digitalize 2,879 lineaments. Digitalization was performed using the vector-based Adobe illustrator drawing software. Image resolution and image size at the nucleus surface range respectively from 0.33–1.23 m per pixel and 0.69–2.79 km. Digitalised lineaments are polyline objects made only of straight line combinations (Supplementary Fig. 2a).

Lineaments were exported in .svg format and projected onto the SPG-SHAP7[25] nucleus model, using the known geometry of OSIRIS images[44] (Supplementary Fig. 2b). A neck axis plane was defined, using the midplane of the neck border coordinates from ref. [25], and the average distance and direction (weighted by segment lengths) of each lineament were computed relative to this.

The fracture cumulative length distribution fit was performed following classic recommendations from ref. [45]. Our dataset is composed of more than 200 measurements and ranges over two orders of magnitude. Nevertheless, to determine power-law exponents, we sampled fractures only inside 0.5% to 25% of the image actual size, in order to avoid typical issues such as: (i) the truncation effect, due to image resolution limits; (ii) the length bias or censoring effect, due to the size of images/sampling area compared to the size of longest fractures; and (iii) a statistical effect due to undersampling of the largest objects.

Cliff directions were computed using the Gocad software (Emerson E&P Software), by drawing lines parallel to the cliffs directly onto the shape model mesh triangles. A parallel/orthographic view was used to avoid perspective/parallax effect bias. The anaglyph 3D view mode was used to estimate depth better, to draw the parallel line on the cliffs accurately, minimizing error in cliff directions.

The full stress tensor for 67 P was computed taking into account gravity and rotational forces, considering a Young's modulus value of 50 MPa and a Poisson ratio of 0.32 (ref. [32]). The stress model was computed using a finite element mesh composed of two million cells, and principal stress values and directions were mapped onto the cg-dlr_spg-shap7-v1.0 model[25].

Data availability

All the images analysed during the current study are available in the ESA-PSA repository (https://archives.esac.esa.int/psa). The data that support the findings of this study are in the Supplementary Information and available from the corresponding author upon reasonable request (matonti@cerege.fr).

References

44. Gaskell, R. W. et al. Characterizing and navigating small bodies with imaging data. *Meteorit. Planet. Sci.* **43**, 1049–1061 (2008).
45. Bonnet, E. et al. Scaling of fracture systems in geological media. *Rev. Geophys.* **39**, 347–383 (2001).